

Flux-flow Josephson oscillator as the broadband tunable terahertz source to open space

Cite as: J. Appl. Phys. **125**, 151603 (2019); doi: [10.1063/1.5070143](https://doi.org/10.1063/1.5070143)

Submitted: 19 October 2018 · Accepted: 5 December 2018 ·

Published Online: 28 March 2019



N. V. Kinev,^{1,a)}  K. I. Rudakov,^{1,2,3} L. V. Filippenko,¹ A. M. Baryshev,³ and V. P. Koshelets¹ 

AFFILIATIONS

¹Kotel'nikov Institute of Radio Engineering and Electronics of RAS, Moscow 125009, Russia

²Moscow Institute of Physics and Technology, Dolgoprudny 141701, Russia

³Kapteyn Astronomical Institute, University of Groningen, 9712 CP Groningen, The Netherlands

^{a)}nickolay@hitech.cplire.ru

ABSTRACT

The flux-flow oscillator (FFO) based on a long Josephson junction has been implemented as a broadband tunable terahertz (THz) source to open space. For this purpose, the transmitting slot antenna has been coupled to the oscillator. Additionally, an elliptical lens with a diameter of 10 mm has been matched to the antenna, forming a narrow output beam of the THz emission. Two designs for the antenna, integrated with the oscillator and developed for operation at different frequency ranges of 0.32–0.55 THz and 0.4–0.7 THz, have been investigated. The FFO has been phase locked to an external reference oscillator by utilizing a harmonic mixer. Its linewidth in the phase-locking regime is determined by the phase noise of the reference oscillator and the number of harmonics used and has been measured to be less than 0.1 MHz. A free-running FFO linewidth from about 2 MHz to several MHz, depending on the operating point, has been obtained. Output emission to open space has been measured by a superconducting integrated spectrometer located in a separate cryostat. The FFO operation as an external source with the achieved emission power and spectral characteristics has demonstrated its applicability for different tasks and purposes where tunable THz sources are required.

<https://doi.org/10.1063/1.5070143>

I. INTRODUCTION

Wideband tunable sources of electromagnetic emission in the terahertz (THz) region are of great importance, since they are required in many fields such as radio physics, astronomy and spectroscopy, medicine, and security systems. The flux-flow oscillator (FFO) based on a long Josephson junction with a length much more than the Josephson penetration depth ($l \gg \lambda_J$) is a promising THz source, due to its excellent operating bandwidth, which can be up to 100% of the central frequency.¹ The FFO was studied experimentally^{1–8} and theoretically^{9–15} and, finally, was utilized as the local oscillator (LO) of the heterodyne THz receiver in the real flight mission TELIS,^{16,17} for atmospheric research. In this mission, as well as in other studies on the FFO and its applications, it was used as an on-chip planar source. It has never been used as a source to open space. The output frequency f is strictly defined by the Josephson equation $hf = 2eV_{DC}$, where h is Planck's constant and V_{DC} is the voltage at the junction. An oscillator based on a Nb/AlN/NbN trilayer with dimensions $16 \times 400 \mu\text{m}^2$ has an operating range from 250 to 750 GHz,¹ corresponding to V_{DC} in the region from

0.52 mV to 1.55 mV. The typical free-running spectral linewidth of the oscillator is of the order of 1 MHz and the line shape is Lorentzian.^{4–6,8} For narrowing the actual spectral line down to a value less than 100 kHz and for collecting in the peak up to 97% of the spectral power (this ratio is called the Spectral ratio), a phase-locking loop (PLL) to the reference oscillator is commonly used. The upper border of the operating frequency range is limited by the gap frequency $2\Delta/h$, which is about 700 GHz for all-Nb junctions, about 1.4 THz for all-NbN junctions and 1.2 THz for all-NbTiN junctions. However, the actual frequency limit of Nb/NbN junctions is usually about 750–850 GHz,^{1,7} due to the high surface resistance of NbN and hence the sharp increase in losses above 750 GHz. These surface losses lead to a decrease of the emitted power due to a damping of the wave propagating along both the tunnel junction and the output transmitting line, and also to a linewidth increase due to a higher differential resistance. For higher frequencies, NbTiN-based junctions are preferable,¹⁸ due to much lower losses at frequencies above 750 GHz so that the upper frequency limit for operation is predicted to be as high as 1–1.2 THz.^{19,20} It should be noted that the

emission frequency range available for FFO applications is also defined by matching structures and other circuit elements usually having narrower bandwidths. The emission power of the FFO is from fractions of $1 \mu\text{W}$ to a few microwatts in magnitude.² This is not large but is quite enough for applications such as heterodyne receiving and spectroscopy. Furthermore, the power can be increased by using a larger current density in the junctions.⁷

II. CONCEPT AND NUMERICAL SIMULATIONS

The main idea of this paper is the on-chip integration of the FFO with the transmitting double-slot lens antenna to provide the FFO emission to open space by using matched transmitting lines. The concept is shown in Fig. 1. The FFO is coupled to the slot antenna via the output microstrip line, as illustrated in Fig. 1(a). Tuning the FFO frequency is equivalent to setting the FFO voltage V_{DC} with the coefficient 483.6 GHz/mV . For setting V_{DC} , two currents are applied: the control line current I_{CL} is used for supplying the magnetic field and can be set typically from 0 mA up to 100 mA and the bias current I_{BIAS} is applied via the FFO tunnel junction. The typical operation bias is from 10 to 30 mA for current densities J_c in the range $3\text{--}10 \text{ kA/cm}^2$. An impedance transformer is used to match the low output impedance of the FFO ($\sim 0.5 \Omega$) and the much higher input impedance of the slot antenna, which is of the order of tens of ohms. Some part of the FFO power is branched to the harmonic mixer (HM), based on the SIS (superconductor-insulator-superconductor) junction and used

in the feedback loop with the oscillator for the phase locking, by means of the PLL system.^{4,8} Another impedance transformer is used to couple the FFO emission to the HM, with an impedance of several ohms. One can choose different FFO operating points at the same frequency (voltage) to optimize the spectral characteristics and the pumping of the HM.

The double-slot antenna is made using a thin film of Nb with a thickness of $\sim 200 \text{ nm}$, which is also the bottom electrode of the FFO, the microstrip lines, and the HM. An SiO_2 insulator with a thickness of 400 nm is used between the top and bottom electrodes. The dimensions of the FFO are $400 \times 16 \mu\text{m}^2$, as was successfully used in previous studies,^{1,16,17} and the HM area is about $1\text{--}1.5 \mu\text{m}^2$. The integrated circuit is fabricated on a Si substrate with a thickness of $D_{\text{Si}} = 0.535 \text{ mm}$ and a dielectric constant of $\epsilon = 11.7$, so the wavelengths in the circuit are $\sqrt{\epsilon} = 3.42$ times smaller than that in vacuum. The length of the antenna slots depends on the frequency range and is about 0.36λ or $1.25\lambda_{\text{Si}}$, where λ and λ_{Si} are the wavelengths in vacuum and in a silicon, respectively, for the central frequency range. The distance between the slots is about 0.1λ or $0.4\lambda_{\text{Si}}$. In Fig. 1(a), the specific design for the $330\text{--}570 \text{ GHz}$ range (central frequency 450 GHz , $\lambda_{\text{Si}} = 195 \mu\text{m}$) is shown. The length of the antenna dipoles is $242 \mu\text{m}$, the width of the slots is $15 \mu\text{m}$, and the distance between the centers of the slots is $75 \mu\text{m}$. This type of antenna has been used in Ref. 21 as the receiving antenna coupled to a SIS detector in the receiver, at 100 GHz , 246 GHz , and 500 GHz . We use this double-slot antenna because of the possibility of locating it maximally close to the FFO and fabricating it in the same technological cycle together with the FFO and HM tunnel junctions.

The chip with the FFO, antenna, and HM integrated circuit is mounted on the back surface of an extended semielliptical lens with a diameter of 10 mm [see Fig. 1(b)] and a far focus distant from the geometrical center of the lens by $D = 1.529 \text{ mm}$. The extension of the lens equals to $D - D_{\text{Si}} = 0.994 \text{ mm}$ so that the center of the antenna is located exactly at the far focus of the lens. The lens and the substrate of the chip are both made of Si to avoid beam refractions on the chip-lens border. It was shown (see Ref. 7) that this type of lens with a matched antenna mounted at its focus can be effectively used over a wide frequency range of $0.1\text{--}1 \text{ THz}$ without changing the lens geometry. Since the FFO is extremely sensitive to external magnetic fields, the circuit is located inside a magnetic shield made of permalloy and copper with a lead layer plated. The shield is open on one side. The shield with the sample is then placed inside a liquid helium (LHe) cryostat with a bath temperature T_{bath} of 4.2 K and a Mylar output window at a room temperature stage. The additional Gortex windows are also used at a 4.2 K and 77 K stages to operate as IR filters, and both Mylar and Gortex windows are transparent in the THz region.

For developing structure designs for different frequency ranges, numerical simulations were performed using specialized software for 3D microwave modeling and optimization. The main task for modeling is the coupling at THz frequencies of the oscillator with a low output impedance to the lens antenna with a higher input impedance and forming the required beam pattern for applications. A simultaneous modeling task is the coupling to the HM based on the SIS junction with some intermediate impedances (higher than the FFO's and lower than the antenna's) in the maximally similar frequency range as for the FFO-to-antenna coupling. Matching to

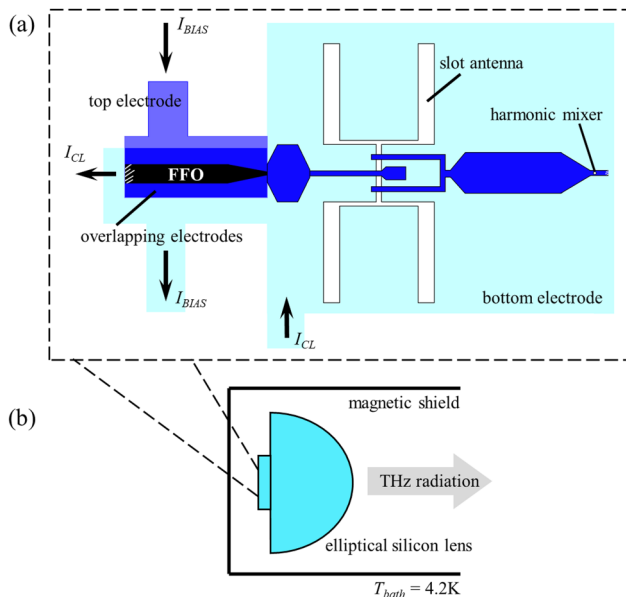


FIG. 1. (a) Layout of the planar microcircuit containing FFO, double-slot antenna, harmonic mixer, and the coupling structures between the elements. Both tunnel junctions, FFO and HM, are to be fabricated using Nb/AlN/NbN or Nb/ AlO_x /Nb trilayers in one technological process; top and bottom electrodes constitute the microstrip lines with an SiO_2 insulator layer. The full dimensions of the slot structure shown are $242 \times 90 \mu\text{m}^2$. (b) Scheme of the chip with the microcircuit shown in (a) placed at the far focus of the lens and inside the magnetic shield.

the antenna should be as high as possible, while matching to the HM should be just enough for proper PLL operation and should not take away much power. Commonly, pumping of the HM at $\sim 5\%$ – 10% of the current jump at the SIS-mixer gap voltage is enough for HM and PLL operations.^{1,5,7} Both couplings should be as wideband as possible for an antenna and transmitting lines of this type. To take into account the superconducting state of the antenna and microstrips, the London penetration depth for thin Nb films $\lambda_L = 85$ nm is used, and the SiO_2 dielectric constant $\epsilon = 4.2$ was taken for thin films. Calculating the real FFO output impedance, which is frequency dependent, is an extremely complicated task due to self-coupling and standing-wave effects,^{15,22} and so the impedance was taken to be constant and equal to 0.5Ω .

It is known from antenna engineering and was also verified during our simulations that the slot antenna bandwidth is usually not more than $\sim 0.5f_0$, where f_0 is the central frequency. At the same time, the FFO operation bandwidth is up to f_0 . Hence, we decided to develop two designs to cover the operating range 0.4 – 0.7 THz. As a result, two designs were numerically simulated: design #1 for $f_0 = 450$ GHz [that is shown precisely in Fig. 1(a)] and design #2 for $f_0 = 600$ GHz. The calculated input impedances of the antenna at the point of connection to the microstrip line for designs #1 and #2 are presented in Fig. 2. One can see that the full impedance dependence is rather flat: it varies between $\sim 30 \Omega$ and $\sim 40 \Omega$ in the target frequency regions. The numerical results for the emission to open space and the coupling with the HM for both designs are illustrated in Fig. 3. The calculations were performed as follows: the emitting edge of the FFO was simulated as the input port (FFO port) with an impedance of 0.5Ω and the HM was simulated as a port (HM port) with an impedance equal to the normal resistance of the junction $R_n = 17.85 \Omega$, corresponding to an area of the junction $A_{HM} = 1.4 \mu\text{m}^2$, based on a trilayer with a normal-state resistance–area product $R_n \times A = 25 \Omega \mu\text{m}^2$.

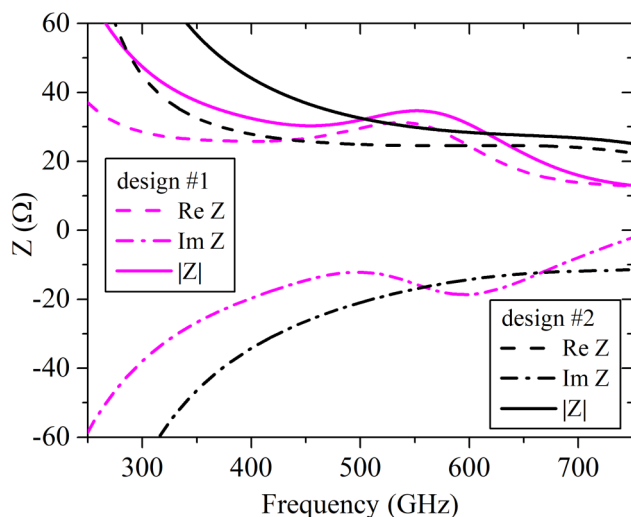


FIG. 2. Input impedance Z of the antenna designs #1 and #2: the real part $\text{Re } Z$, the imaginary part $\text{Im } Z$, and the full impedance $|Z|$ are shown.

The capacity of the HM was taken into account by embedding a capacitor according to the specific capacitance of the tunnel trilayer taken as $85 \text{ fF}/\mu\text{m}^2$ in the model.

The microstrip line after the HM contains the rf short based on a radial stub and then transforms to a CPW line for proper connection to the contact pads. The simulation program calculates the power absorbed by the HM port from the transmitting line P_{HM} at each frequency (dashed lines in Fig. 3) and the power returned to the input FFO port P_{return} . Hence, the power coupled to the whole integrated output structure is $P_{couple} = 1 - P_{return}$ (dashed-dotted line) and the power emitted to open space is $P_{emit} = 1 - P_{return} - P_{HM} = P_{couple} - P_{HM}$ (solid line). All the power values are normalized to the FFO output power. Additional computation of the far-field distribution simulated by the program showed that all the constituents of the FFO power were taken into consideration; in particular, only about 1% – 2% of the power at operating frequencies passed out via the rf short. According to the numerical simulation, the operating frequency ranges of the antenna, evaluated as the ranges with emission above 0.7 of FFO total power, are 320 – 550 GHz for design #1 and 400 – 700 GHz for design #2. Thus, the two designs cover the range 0.32 – 0.7 THz. Further fabrication of the samples and experimental research details is reported in Sec. III.

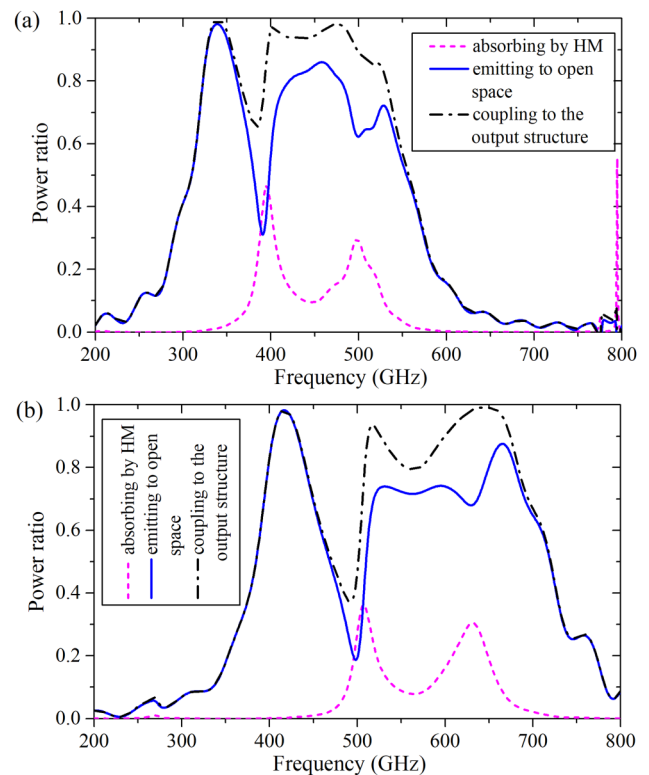


FIG. 3. FFO power absorbed by the harmonic mixer (dashed line), emitted to open space (solid line), and absorbed by the full output structure (dashed-dotted line), normalized to the total output power (a) for design #1 and (b) for design #2.

III. EXPERIMENT

A. Samples preparation

The technology in our group for fabrication of samples containing integrated circuits with all-Nb and Nb/NbN tunnel junctions, with approximately micrometer and submicrometer dimensions, has been described elsewhere.^{23,24} The key technology processes are electron-beam lithography for mask preparation, magnetron sputtering, and “lift-off” lithography. In this study, 4×4 -mm² chips with designs #1 and #2 containing the FFO and HM based on Nb/AlN/NbN trilayers were fabricated on a silicon substrate. According to DC testing, the tunnel junctions of the batch have a normal-state resistance–area product $R_n \times A \sim 18 \Omega \mu\text{m}^2$, which corresponds to a current density of $J_c \sim 12 \text{ kA/cm}^2$. The gap voltage V_g is about 3.45–3.55 mV and the quality factor, defined as the sub-gap resistance to normal-state resistance ratio R_g/R_n , is about 30, which is a good result for the NbN technique.

For testing at THz frequencies, the chip is then stuck to the lens as shown in Fig. 1(b) and bonded to the bias plate by aluminum wires utilizing ultrasonic bonding. The six contact pads are used for fully controlling the FFO with a four-point biasing current-control scheme ($+I_{BIAS}$, $+V_{BIAS}$, $-I_{BIAS}$, $-V_{BIAS}$) and an additional two-point control line scheme for applying the magnetic field ($+I_{CL}$, $-I_{CL}$). The HM is controlled via a four-point biasing voltage-control scheme. Two additional transmitting lines to the chip are used: one for supplying the reference rf signal of about 20 GHz to the HM and for measuring the output intermediate frequency (IF) signal and the other for applying the feedback signal to the FFO from the PLL system. The final cryogenic module with the chip on the lens, bias plate with DC and rf wiring inside the magnetic shield, is mounted inside the cryostat opposite the output window.

B. Measurement setup

A complex block diagram of the setup for measuring the FFO emission to open space is shown in Fig. 4. Two liquid helium (LHe) cryostats are used for the oscillator and the receiver: the left part of the diagram shows the “emitting” cryostat (#1) and the right part shows the “receiving” cryostat (#2). The schematics of

the FFO microcircuit design is discussed in Sec. II. Signals from the FFO and n th harmonics from the synthesizer at 19–21 GHz are mixed by the HM. The intermediate frequency (IF) signal from the HM in the range 0–800 MHz is amplified first by the cryo-amplifier based on a high electron mobility transistor (HEMT) and then by the room temperature amplifier. It is then branched to a PLL system and to spectrum analyzer (SA) #1 for direct reading of the FFO spectra. The main part of the FFO output power is coupled to the slot antenna and radiated to open space and then directed to the THz spectrometer based on the superconducting integrated receiver (SIR). The SIR operation (the whole right part of the diagram in Fig. 4) has previously been discussed in Refs. 5 and 25. One should note that two FFOs are used in the experimental setup: one (FFO #1) is the object of the study and the other (FFO #2) is used as the local oscillator (LO) of the SIR. Since the SIR IF frequency range is 4–8 GHz and the FFO frequency is strictly defined by the Josephson voltage, for the SIR to receive the emitting signal, the voltages of the FFOs should be distant from one another within the range 8.3–16.5 μV . The backend of the SIR is SA #2, which immediately shows the receiving signal converted down to the IF range. Since the gains of the amplifiers in the IF chain of the HM in cryostat #1 and in the IF chain of the SIS mixer in cryostat #2 are different, the spectra detected by spectrum analyzers #1 and #2 should not be compared by power. Nevertheless, they can be compared by shape, taking into account the fact that the spectrum detected by SA #1 is the convolution of FFO #1 signal and the n th harmonic of the synthesizer (assumed to be a δ -function), while the spectrum detected by SA #2 is the convolution of the two FFO signals, at least one of which (#2) should be phase locked during the measurements, forming a signal close to a δ -function.

C. Results and discussion

A set of the current-voltage curves (IVCs) of fabricated FFOs measured for different magnetic fields produced by I_{CL} in the range 20–90 mA with a step size of 2 mA (36 curves altogether), is presented in Fig. 5(a). The bottom axis of frequency strictly corresponds to the top axis of the voltage. The set is quite similar to the IVCs previously obtained in Ref. 1 for Nb/AlN/NbN-based FFOs, except for the slope of the IVCs (high differential resistance) and

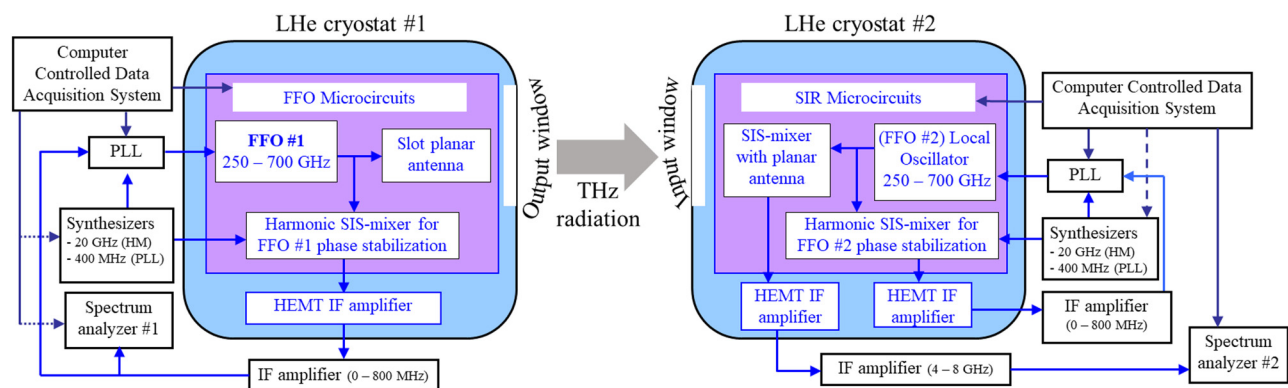


FIG. 4. Block diagram of the experimental setup for studying the FFO emission to open space using a THz spectrometer based on a superconducting integrated receiver.

therefore the absence of clearly expressed Fiske steps^{1,5} and also the gap in operating points at currents from 13 mA to 22 mA between ~ 400 GHz and ~ 490 GHz. Both features are the consequence of disadvantages in the present control line design, which will be remodeled in the future. In addition, the J_c of the batch turned out to be higher than expected: 12 kA/cm^2 instead of $7\text{--}8.5 \text{ kA/cm}^2$. This also led to a stronger slope in the IVCs and degradation of Fiske steps. Nevertheless, neither the slope nor the lack of operating points in some regions of the IVCs affects the fundamental Josephson oscillation or the frequency characteristics of the antenna design and the transmission lines. The pumping of the SIS-based HM by the FFO power leads to the appearance of the quasiparticle step I_{pump} on the IVC of the HM, which is measured directly over the whole frequency range of the FFO operation. In Fig. 5(b), the experimental results for the frequency dependence of the normalized HM

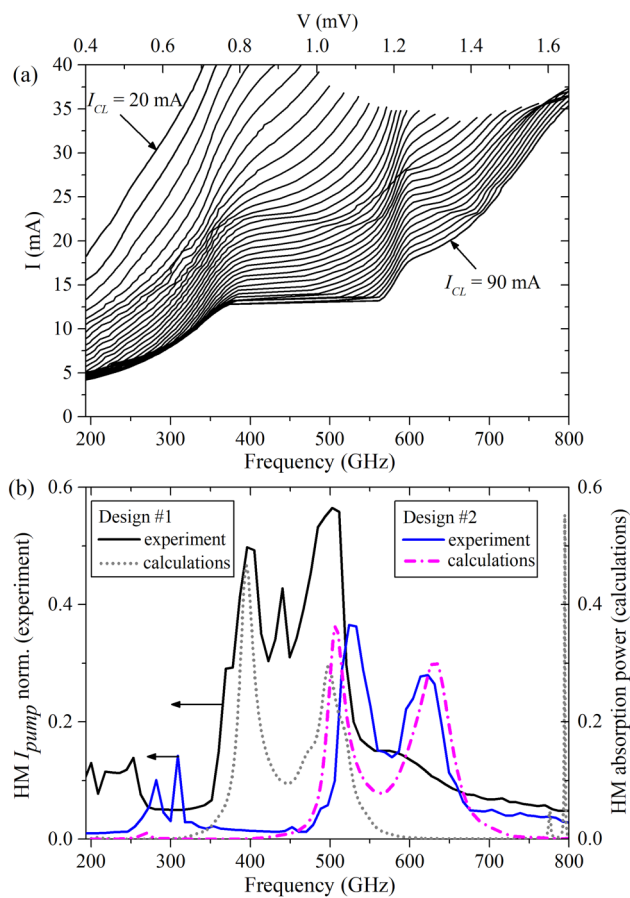


FIG. 5. (a) IVCs of the FFO with the dimensions $400 \times 16 \mu\text{m}^2$ measured for different magnetic fields produced by the control line current with an I_{CL} step of 2 mA. (b) Experimental results of HM pumping by the FFO power and calculation results of the FFO power absorbed by the HM port. The I_{pump} is normalized to the “current jump” at the SIS gap voltage, equal to $206 \mu\text{A}$ for the HM in design #1 and $199 \mu\text{A}$ for the HM in design #2. The HM absorption power is normalized to the total FFO output power.

pumping current are presented together with the calculation results for the absorbed power for designs #1 and #2 [shown earlier by dashed lines in Figs. 3(a) and 3(b)]. The axes of frequency in (a) and (b) are exactly one above the other, for clarity. There is a good agreement between the experiment and the numerical simulations.

The spectral characteristics of the FFO were measured both by SA #1 (on-chip emission) and by SA #2 (open-space emission detected by the SIR). The typical spectra are shown in Fig. 6 for design #2 at 590 GHz. Free-running and phase-locked spectral lines measured in the upper sideband are presented. As can be seen, the linewidths of free-running spectra are almost similar (red and magenta lines). The IF power levels of spectral lines are quite different due to different gains of IF circuits, as mentioned in Sec. III B. The phase-locked line measured by SA #2 (gray line) seems to be wider than that measured by SA #1 (black line) due to the different resolution bandwidths (RBW) of the analyzers. The linewidth of the phase-locked spectra in Fig. 6 is completely defined by the RBW of SA (see, for example, figures shown in previous publications,^{4,6} Fig. 2 and Fig. 5, respectively, therein) and proved to be about 100 kHz when $\text{RBW} = 100 \text{ kHz}$ is used during the measurements. The actual linewidth of the phase-locked spectra is defined by the phase noise of the

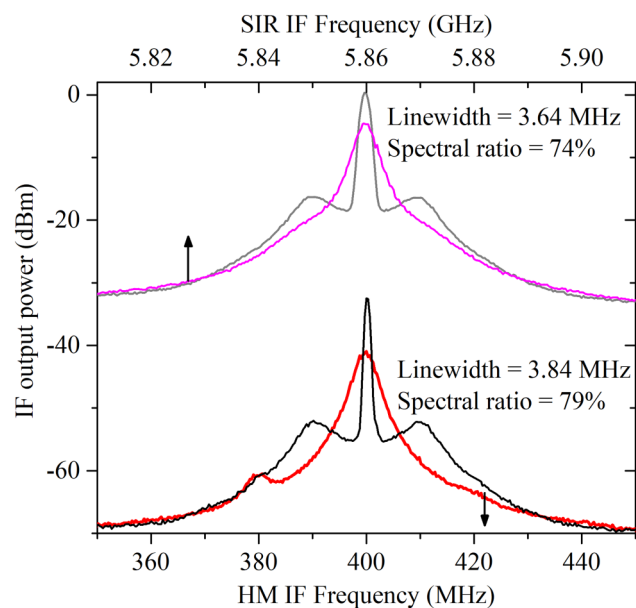


FIG. 6. Power spectra of the FFO at a frequency of 590 GHz for the sample with design #2 measured using the on-chip HM (SA #1)—free-running (red line) and phase-locked (black line) spectra, and measured using the SIR (SA #2)—free-running (magenta line) and phase-locked (gray line) spectra. The bottom and top axes of frequency represent the different IF ranges of 0–800 MHz for the on-chip HM IF and 4–8 GHz for the SIR IF. The span for both axes is the same, 100 MHz, and all the spectra are measured in the upper sideband. An estimated linewidth for the free-running spectra and a spectral ratio for the phase-locked spectra are shown near the curves. The resolution bandwidths of the analyzers are different: 1 MHz for SA #1 and 1.8 MHz for SA #2. For the spectra measured by SIR (magenta and gray lines), the LO of the SIR, FFO #2, is phase locked.

TABLE I. Main results of the FFO emission measurements to the open space by the SIR.

Sample	R_n of the HM (Ω)	Operating frequency of the FFO emission to open space (GHz)	The best free-running linewidth obtained at this frequency (MHz)	Signal-to-noise ratio (dB)	SIR LO phase locking ability (+ or -)
Sample with design #1	13.6	387	2.5	29.8	-
		392	3.2	25.2	-
		497	14.5	21.7	+
		505	4.0	27.4	+
		536	10.1	20.1	+
		540	2.7	29.6	+
		572	2.7	27.2	+
		592	3.4	23.3	+
		600	12.8	20.4	+
		650	13.6	17.6	+
Sample with design #2	14.8	518	5.9	28.0	+
		550	8.6	29.9	+
		560	4.3	30.1	+
		580	2.5	28.4	+
		590	3.6	30.0	+
		600	12.9	22.8	+
		620	29.1	15.2	+
		650	16.1	20.2	+
		670	10	22.3	+
		690	5.6	23.4	+
		700	7	23.1	+
		720	7.5	16.3	-
		730	10.6	13.0	-
		735	8.9	12.2	-

synthesizer used multiplied by n^2 , where n is the number of harmonics. The spectral ratio defined for a phase-locked line as the percentage of the power concentrated in the peak is a little less in the case of measurement by the SIR, also due to the higher RBW of SA #2.

The two samples, design #1 and design #2, were carefully studied in their operating frequency ranges. The measurements as shown in Fig. 6 were carried out at many different frequencies, and the results are summarized in Table I. The linewidth at many of the studied operating points is not as good as may be desired—typically above 5 MHz—due to the high J_c leading to a strong slope in the FFO IVCs (high differential resistance). This issue can be solved simply by fabricating another batch with more appropriate trilayer parameters. Hence, one should not consider such values to be representative for the FFO. In many previous papers, a linewidth of about 1–2 MHz is obtained for the Fiske steps IVC region (lower than $V_{gap}/3$) and of about 4–7 MHz for the true flux-flow regime (above $V_{gap}/3$).^{4,6,8,16} We emphasize that the main results of this research are the detection of the FFO emission to open space and demonstration of the similar spectral properties for on-chip radiation and open-space radiation, regardless of the measurement technique. Therefore, the best obtained results for the properties of the FFO as an on-chip oscillator can be repeated for FFO as an open-space oscillator. As for the frequency operating ranges, which were calculated to be 320–550 GHz for design #1 and 400–700 GHz for design #2 (using the level of 0.7 of total FFO power), the experimental results

confirmed the numerical simulations (see Table I). The exception to this confirmation is the case of frequencies outside the SIR operating range of 450–700 GHz. Thus, the operating frequencies 320–450 GHz for design #1 and 400–450 GHz for design #2 could not be studied accurately by the SIR. Nevertheless, even outside the SIR operating range, the emission at some frequencies was registered without stabilization of the SIR LO (FFO #2), e.g., at 387 GHz and 392 GHz for design #1 and at 720 GHz, 730 GHz, and 735 GHz for design #2. In these cases, the FFO spectral linewidth could still be measured using the on-chip HM, provided the oscillator could be phase locked.

A beam pattern for the lens antenna was not measured accurately because a complex optical experimental setup is required, and the pattern of the receiver must also be taken into account. We made a rough estimate for the width of the central beam lobe of about a few degrees, by manually moving and rotating cryostat #1 relative to cryostat #2. Enlarging the distance between the cryostat windows from 6 cm to 30 cm had almost no influence on the receiving power, but rotating the output window by 1°–2° from the central position (defined as the maximum power position) leads to a sharp decrease in receiving power. This result is as expected, because the elliptical silicon lens used for the oscillator is the same as that used for the SIR, where the lens is coupled to a double-dipole receiving antenna. It is the lens that mostly defines the beam pattern of such lens antenna systems. The beam diagram for the

SIR optics has been presented in Refs. 5 and 16 (Fig. 13 and Fig. 3, respectively, therein) for the samples for the TELIS flight mission. All the spectral measurements in this paper are made by manually tuning the relative positions of the “emitting” and “receiving” cryostats to obtain the maximum receiving signal.

The concept of integrating the FFO with the antenna on a single chip turned out to be a very good perspective for developing a tunable THz source emitting the open space. The main issue for such a source needed a specific frequency or frequency range is the designing of the antenna and the transmitting line structures between the FFO, the antenna, and the HM. From the point of view of producing devices for practical use, some directions for future developments are planned. The first is the widening of the operation range, in both the lower and upper frequencies. The lower frequency border of the present samples of the FFO is about 200–250 GHz, so the output structures are to be coupled to the oscillator at these frequencies. The upper frequency limit is defined by the gap frequency and can potentially reach 1–1.2 THz if NbTiN-based junctions and transmitting lines are used.^{19,20} For both upper and lower frequency ranges, another experimental setup based on the Golay cell or the Si bolometer should be used for detecting the THz emission, since such frequencies are outside the SIR operating region. The second direction is the redesigning of the FFO control line and fabrication of samples with a more appropriate current density, to avoid the gap at the points of operation below $V_{gap}/3$ on the IVCs and to provide continuous frequency tuning with a free-running spectral linewidth of not more than 5–7 MHz over the whole range. Finally, the third direction is the accurate measurement of the calibrated emission power and the beam pattern of the oscillator. For calibrated power measurements, a Golay detector or THz bolometer could be used.

IV. CONCLUSION

We elaborated upon the idea for the THz source based on the FFO and developed devices for two frequency ranges that emit to open space at a tunable frequency in the ranges of 0.32–0.55 THz and 0.4–0.7 THz, which cover the 0.32–0.7 THz region. The slot lens antenna is used for providing the emission from the chip surface to open space. A small part of the FFO power (~10%–20%) is branched to the harmonic mixer for phase locking of the oscillator, using the feedback locking loop. Numerical simulations for the sample designs were undertaken, and samples based on Nb/AlN/NbN Josephson junctions with a gap voltage of ~3.5 mV were fabricated and experimentally studied. Emission to open space was successfully obtained and measured using a superconducting spectrometer located in a separate cryostat. The spectral lines of the FFO emission with a signal-to-noise ratio of up to 30 dB and a free-running linewidth as low as a few megahertz were obtained. At the same time, the measured linewidth of the phase-locked oscillator is defined by the resolution bandwidth of the spectrum analyzer, down to a value of 100 kHz,^{4,6} while the actual linewidth is determined by the phase noise of the reference oscillator multiplied by the square of the number of harmonics. The experimental results for the frequency ranges of the open-space emission and of the HM pumping by the FFO are in good agreement with the numerical simulations.

ACKNOWLEDGMENTS

The development, fabrication, and experimental measurements of the samples were supported by the Russian Science Foundation (Project No. 17-79-20343). The adjustment of the cryostats in the experimental setup (Sec. III B) was supported by the RFBF (Project No. 17-52-12051).

REFERENCES

- 1M. Y. Torgashin, V. P. Koshelets, P. N. Dmitriev, A. B. Ermakov, L. V. Filippenko, and P. A. Yagoubov, *IEEE Trans. Appl. Supercond.* **17**, 379 (2007).
- 2T. Nagatsuma, K. Enpuku, F. Irie, and K. Yoshida, *J. Appl. Phys.* **54**, 3302 (1983).
- 3A. V. Ustinov, J. Mygind, and V. A. Oboznov, *J. Appl. Phys.* **72**, 1203 (1992).
- 4V. P. Koshelets, S. V. Shitov, L. V. Filippenko, V. L. Vaks, J. Mygind, A. M. Baryshev, W. Luinge, and N. Whyborn, *Rev. Sci. Instrum.* **71**, 289 (2000).
- 5V. P. Koshelets and S. V. Shitov, *Supercond. Sci. Technol.* **13**, R53 (2000).
- 6V. P. Koshelets, S. V. Shitov, P. N. Dmitriev, A. B. Ermakov, L. V. Filippenko, V. V. Khodos, V. L. Vaks, A. M. Baryshev, P. R. Wesselius, and J. Mygind, *Physica C* **367**, 249 (2002).
- 7S. Kohjiro, Z. Wang, S. V. Shitov, S. Miki, A. Kawakami, and A. Shoji, *IEEE Trans. Appl. Supercond.* **13**, 672 (2003).
- 8V. P. Koshelets, P. N. Dmitriev, A. B. Ermakov, A. S. Sobolev, M. Y. Torgashin, V. V. Kurin, A. L. Pankratov, and J. Mygind, *IEEE Trans. Appl. Supercond.* **15**, 964 (2005).
- 9T. Nagatsuma, K. Enpuku, K. Sueoka, K. Yoshida, and F. Irie, *J. Appl. Phys.* **58**, 441 (1985).
- 10J. Mygind, V. P. Koshelets, M. R. Samuelsen, and A. S. Sobolev, *IEEE Trans. Appl. Supercond.* **15**, 968 (2005).
- 11A. L. Pankratov, V. L. Vaks, and V. P. Koshelets, *J. Appl. Phys.* **102**, 063912 (2007).
- 12A. L. Pankratov, *Appl. Phys. Lett.* **92**, 082504 (2008).
- 13E. A. Matrozova, A. L. Pankratov, M. Y. Levichev, and V. L. Vaks, *J. Appl. Phys.* **110**, 053922 (2011).
- 14E. A. Matrozova, A. L. Pankratov, and L. S. Revin, *J. Appl. Phys.* **112**, 053905 (2012).
- 15D. R. Gulevich, V. P. Koshelets, and F. V. Kusmartsev, *Phys. Rev. B* **96**, 024515 (2017).
- 16G. Lange, D. Boersma, J. Dercksen, P. Dmitriev, A. B. Ermakov, L. V. Filippenko, H. Golstein, R. Hoogeveen, L. de Jong, A. V. Khudchenko, N. V. Kinev, O. S. Kiselev, B. Kuik, A. de Lange, J. Rantwijk, A. S. Sobolev, M. Y. Torgashin, E. Vries, P. A. Yagoubov, and V. P. Koshelets, *Supercond. Sci. Technol.* **23**, 045016 (2010).
- 17V. P. Koshelets, P. N. Dmitriev, M. I. Faley, L. V. Filippenko, K. V. Kalashnikov, N. V. Kinev, O. S. Kiselev, A. A. Artanov, K. I. Rudakov, A. de Lange, G. de Lange, V. L. Vaks, M. Y. Li, and H. B. Wang, *IEEE Trans. Terahertz Sci. Technol.* **5**, 687 (2015).
- 18J. W. Kooi, J. A. Stern, G. Chattopadhyay, H. G. LeDuc, B. Bumble, and J. Zmuidzinas, *Int. J. Infrared Millim. Waves* **19**, 373 (1998).
- 19J. Kawamura, J. Chen, D. Miller, J. Kooi, J. Zmuidzinas, B. Bumble, H. G. Leduc, and J. A. Stern, *Appl. Phys. Lett.* **75**, 4013 (1999).
- 20B. D. Jackson, A. M. Baryshev, G. de Lange, J.-R. Gao, S. V. Shitov, N. N. Iosad, and T. M. Klapwijk, *Appl. Phys. Lett.* **79**, 436 (2001).
- 21D. F. Filipovic, S. S. Gearhart, and G. M. Rebeiz, *IEEE Trans. Microw. Theory Tech.* **41**, 1738 (1993).
- 22A. L. Pankratov, A. S. Sobolev, V. P. Koshelets, and J. Mygind, *Phys. Rev. B* **75**, 184516 (2007).
- 23L. V. Filippenko, S. V. Shitov, P. N. Dmitriev, A. B. Ermakov, V. P. Koshelets, and J. R. Gao, *IEEE Trans. Appl. Supercond.* **11**, 816 (2001).
- 24A. Khudchenko, A. M. Baryshev, K. I. Rudakov, P. M. Dmitriev, R. Hesper, L. Jong, and V. P. Koshelets, *IEEE Trans. Terahertz Sci. Technol.* **6**, 127 (2016).
- 25O. Kiselev, M. Birk, A. Ermakov, L. Filippenko, H. Golstein, R. Hoogeveen, N. Kinev, B. Kuik, A. Lange, G. Lange, P. Yagoubov, and V. Koshelets, *IEEE Trans. Appl. Supercond.* **21**, 612 (2011).